

Predictive 3D modelling of free oblique cutting of Ti6Al4V titanium alloy and experimental validation for a wide range of conditions

[FD:] Include AI?

F. Ducobu^{a,*}, O. Pantalé^b, E. Rivière-Lorphèvre^a, B. Lauwers^c

^a*Machine Design and Production Engineering Lab, Research Institute for Science and Material Engineering, UMONS, Belgium*

^b*Laboratoire Génie de Production, INP/ENIT, Université de Toulouse, Tarbes, France*

^c*Department of Mechanical Engineering, KU Leuven & Flanders Make@KU Leuven-MaPS, Belgium*

Abstract

Modelling of the cutting process needs to move from a 2D to a 3D configuration to get closer to industrial applications. The study introduces a predictive 3D finite element model of free orthogonal and oblique cutting with an ANN-based material constitutive model and experimental validation in strictly the same conditions (cutting and geometrical). Predictive performance of the model is high for the forces in the 3 directions and the chip thickness ratio on all 36 cutting conditions (including 2 inclination angles). Accuracy of the main cutting force is excellent: the mean difference with the experiments is 3%.

[FD:] Review and update

Keywords:

Oblique cutting, Finite element method (FEM), Predictive model, Artificial Neural Network (ANN)

1. Introduction

2 Selection of the tools and the cutting conditions in machining, but also com-
3 prehension of the influence of the process parameters on the quality of a compo-

*Corresponding author. Tel.: +32 65 45 68

Email address: Francois.Ducobu@umons.ac.be (F. Ducobu)

4 nent and its optimisation, are still difficult to achieve because of the high level
5 of complexity and linked nonlinear phenomena. In the frame of digital manu-
6 facturing and Industry 4.0, modelling of the cutting process supports them, while
7 remaining a challenging task. As highlighted by Arrazola et al. [1], most finite el-
8 ement (FE) models are developed in 2D (orthogonal cutting configuration usually)
9 although industrial applications require a 3D modelling.

10 Experimental validation of a model is a crucial step in the modelling of the
11 cutting process. The experimental configuration must be as close as possible to
12 the simulation. For orthogonal cutting validation, a rotating movement usually
13 generates the cutting speed. This is often achieved in turning [2] or in milling
14 [3] and the diameter of the rotating part must be large enough to reduce the in-
15 fluence of the curvature on the results. Experimental configurations in strictly
16 orthogonal cutting conditions are less often adopted, for example, in broaching
17 [4] or milling [5, 6] machines. While they remove assumptions linked to the ro-
18 tating cutting movement, they usually allow for lower cutting speeds (except on
19 a dedicated machine, such as in Afrasiabi et al. [7]). Free oblique cutting with a
20 straight cutting edge has not been studied yet: all the efforts have been focussing
21 on orthogonal cutting (mostly for 2D validation).

22 Lagrangian and Eulerian formulations are the most used for FE modelling of
23 the cutting process. Combinations of formulations, such as Arbitrary Lagrangian-
24 Eulerian (ALE) and Coupled Eulerian-Lagrangian (CEL) are increasingly used to
25 avoid (or reduce) mesh distortions [8]. The Coupled Eulerian-Lagrangian (CEL)
26 formulation has recently been successfully applied to the modelling of cutting (2D
27 orthogonal configuration): it provides accurate results with a realistic chip shape
28 and no mesh distortion [8]. First applications in 3D are found in recent works
29 [3, 9–12]. They cover (free) orthogonal cutting or a simple 3D operation, while
30 free oblique cutting still needs to be investigated.

The behaviour of the machined material is one of the key aspects of a FE model
[1, 13]. Research is very intense in this field, which leads to a growing number
of material constitutive models ranging from empirical to physical models, some
including microstructure effects [13]. The thermo-elasto-viscoplastic empirical
model of Johnson-Cook (JC) [14] is still the most used so far:

$$\sigma^y = \left(A + B \varepsilon^{p^n} \right) \left(1 + C \ln \frac{\dot{\varepsilon}^p}{\dot{\varepsilon}_0^p} \right) \left(1 - \left[\frac{T - T_{\text{room}}}{T_{\text{melt}} - T_{\text{room}}} \right]^m \right) \quad (1)$$

31 The flow stress, σ^y , is a function of the plastic strain, ε^p , of the plastic strain rate,
32 $\dot{\varepsilon}^p$, and of the temperature, T . It is composed of 3 terms describing independently

plastic, viscous and thermal aspects. One of the points in favour of its adoption is the rather limited number of parameters to be identified, 5: A , B , C , m and n . $\dot{\epsilon}_0^P$ is the reference plastic strain rate, while T_{room} and T_{melt} are the room temperature and the melting temperature, respectively. More recent models developed based on it, such as the one of Calamaz et al. [15], increase this number of parameters (for Calamaz's particular model to 9). The better (in theory) description of the behaviour is achieved at the cost of greater complexity of the identification process and of a reduction of the link with the physical meaning of the model. When a continuous chip is formed, JC model has moreover proved to be well-suited [].

One issue of material behaviour modelling for cutting simulation is the identification of the model parameters, moreover as the experimental equipment does not allow to reach the high levels of strains, strain rates and temperature of machining [13]. Inverse identification is an alternative, but the uniqueness of the solution is not always guaranteed [1, 13]. The early work of Özel and Altan [16] used the least squares method to inversely identify the input parameters of a FE model. Shrot and Bäker [17] then used the Levenberg–Marquardt algorithm for their identification of the constitutive material parameters. They showed that similar results (cutting forces and chip morphology) could be obtained by different sets of parameters and therefore highlighted the non-uniqueness of the solution of the inverse problem. In addition to the flow stress parameters, Klocke et al. [18] also identified the damage parameters. In more recent works, such as Bosetti et al. [19] and Denkena et al. [20], the approach to tackle the inverse identification problem is moving from optimisation to Artificial Intelligence (AI) based methods. The Downhill Simplex Algorithm (DSA) is adopted by Bergs et al. [21] and by Hardt et al. [22] for AISI 1045. Stampfer et al. [23] also selected the DSA when dealing with AISI 4140 tempered at 3 different temperatures. In [24], Hardt et al. showed that the Particle Swarm Optimization (PSO) was more efficient to solve the inverse problem than the Downhill Simplex Algorithm, even if computation time is still significant. In an effort to reduce it, an Efficient Global Optimization (EGO) algorithm has recently been introduced by Kugalur Palanisamy et al. [25]. They simultaneously identified the parameters of the material constitutive model and of the friction model for Ti6Al4V. Most of these works highlight the non-uniqueness of the identification and they all require the definition of the analytical expression of the constitutive model.

This paper fills the literature gap on oblique cutting by investigating free orthogonal and oblique 3D cutting configurations from both the experimental and the numerical points of view. An Artificial Neural Network (ANN), introduced in Pantalé et al. [26], is implemented in a FE cutting model for the first time in-

stead of the analytical JC law. A broad range of cutting speeds (6), uncut chip thicknesses (3) and inclination angles (2) resulting in 36 different conditions are considered to demonstrate the predictive ability of the FE model for fundamental variables. No assumption is made about the geometry of the machined workpiece in the model (i.e. its width is the same as in the experiments), while keeping computation time relevant for industrial applications. The developments apply to the titanium alloy Ti6Al4V.

2. Experimental setup

A 3-axis GF Mikron VCE 600 Pro milling machine is used to carry out dry free orthogonal and oblique cutting tests on Ti6Al4V (grade 5 annealed at 750°C for 1 h followed by air cooling) with the same kinematics as a shaper. As shown in Figure 1, the tungsten carbide tool (modified LCGN160602-0600-FG, CP500 from SECO) is fixed on a dedicated holder (modified CFHN-06 from SECO) and the sample to be cut is clamped in the spindle (no rotation is allowed during the test). The top of the sample includes 3 ribs of 1 mm in width (width of the tool is 6 mm) and 10 mm in length. The test consists of removing the upper layer (its height is the uncut chip thickness, h) of one rib at the prescribed cutting speed, v_c . The cutting speed is provided by the feed rate, v_f , of the machine (max. value of 40 m/min). The tool cutting edge inclination, λ_s , results from the relative angular orientation of the tool and the sample. Table 1 shows the cutting conditions: 6 cutting speeds, 3 uncut chip thicknesses and 2 inclination angles, each is repeated 3 times.

Forces are measured with a 3-component Kistler 9257B dynamometer and are amplified by a Kistler 5070A charge amplifier. Acquisition is performed at 3 kHz with a Kistler 5697A2 data acquisition system and the DynoWare software. Recorded forces are then filtered with a second-order low-pass Bessel filter at 750 Hz before computing the mean value of the signal at steady state.

All the chips are collected and observed with a Dino Lite digital microscope AM7013MZT (5 MP, magnification 20× – 250×). Each chip is measured 3 times along its length to get a mean value representative of the whole chip.

3. Finite element model

3.1. Modelling choices

The CEL formulation is adopted to model the dry free orthogonal and oblique cutting tests with Abaqus/Explicit 2020. The 3D model is composed of a fixed

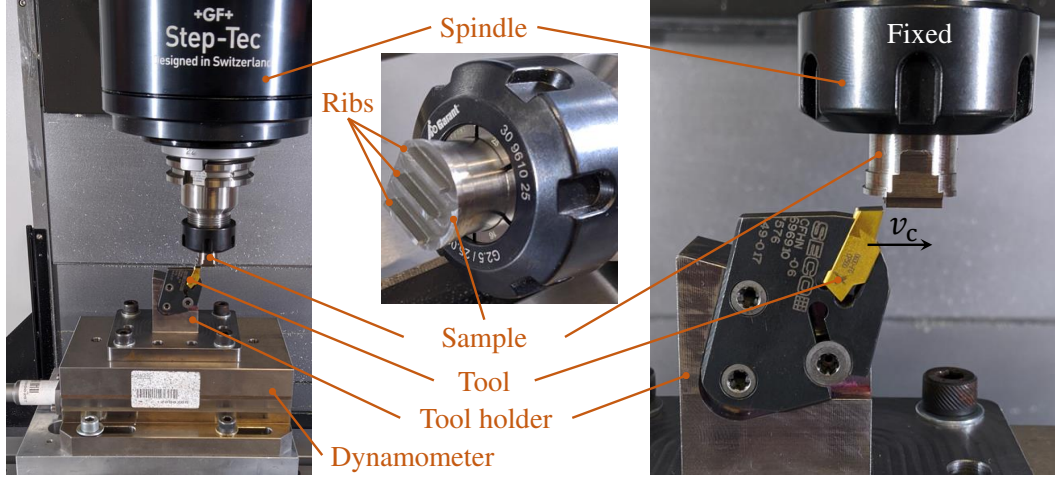


Figure 1: Experimental setup

Table 1: Cutting conditions of the study

Parameter	Values
Cutting speed, v_c (m/min)	5, 7.5, 10, 20, 30, 40
Uncut chip thickness, h (μm)	40, 60, 80
Cutting edge inclination, λ_s ($^\circ$)	0, 6
Width of the workpiece (mm)	1
Length of the workpiece (mm)	10
Width of the cutting edge (mm)	6 (1.1 in the model)
Cutting edge radius, r_β (μm)	20
Rake angle, γ_0 ($^\circ$)	15
Clearance angle, α_0 ($^\circ$)	2

105 Lagrangian tool and a Eulerian workpiece (Figure 2). Chip formation occurs by
 106 plastic flow across the Eulerian domain with no mesh distortion. The Eulerian for-
 107 mulation enables to form chips without damage properties, removing modelling
 108 assumptions. These two characteristics contribute to cutting models providing
 109 accurate results and realistic chips [8].

110 As shown in Figure 3, the full width of the workpiece, i.e. a rib in the exper-
 111 iments, (1 mm) is modelled. To allow chip formation and side flow, the Eulerian
 112 domain is wider (it includes the volume in which material can move). The vol-

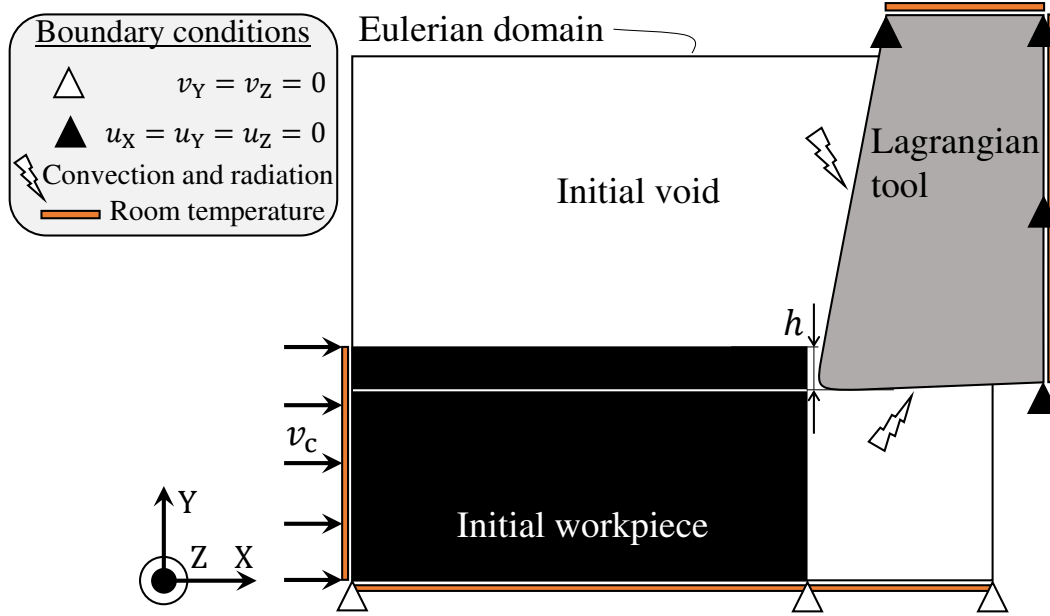


Figure 2: Boundary conditions and schematic initial geometry of the model

ume above the initial workpiece is also meshed with Eulerian elements for the same reasons. As in the experiments and to fulfil the hypothesis of free orthogonal and oblique cutting, the tool is wider than the workpiece (it is of 1.1 mm in the model and of 6 mm in the experiments). It is very important to stress that the models are the same for both inclination angles: they only differ by the rotation of the tool of 6° about Y axis as in the experiments (Figure 3). This, coupled to the absence of assumptions when developing the models, contributes to make the models predictive: no input is changed when cutting conditions do.

According to a previous mesh sensitivity study in orthogonal cutting with the CEL formulation [9], elements edge size is $5\text{ }\mu\text{m}$ in the plane parallel to the cutting speed. In the direction perpendicular to this plane, it is $5\text{ }\mu\text{m}$ in areas close to the lateral boundaries of the Eulerian domain and $50\text{ }\mu\text{m}$ in the middle of the workpiece. To reduce computation time, the size of the model depends on the value of the uncut chip thickness. This results in a Eulerian domain (EC3D8RT linear 3D Eulerian elements with 8 nodes, coupled mechanical-thermal behaviour and reduced integration) composed of 216,550 to 273,350 nodes and a Lagrangian domain (C3D8T linear 3D Lagrangian elements with 8 nodes, coupled mechanical-thermal behaviour) of 4,650 nodes.

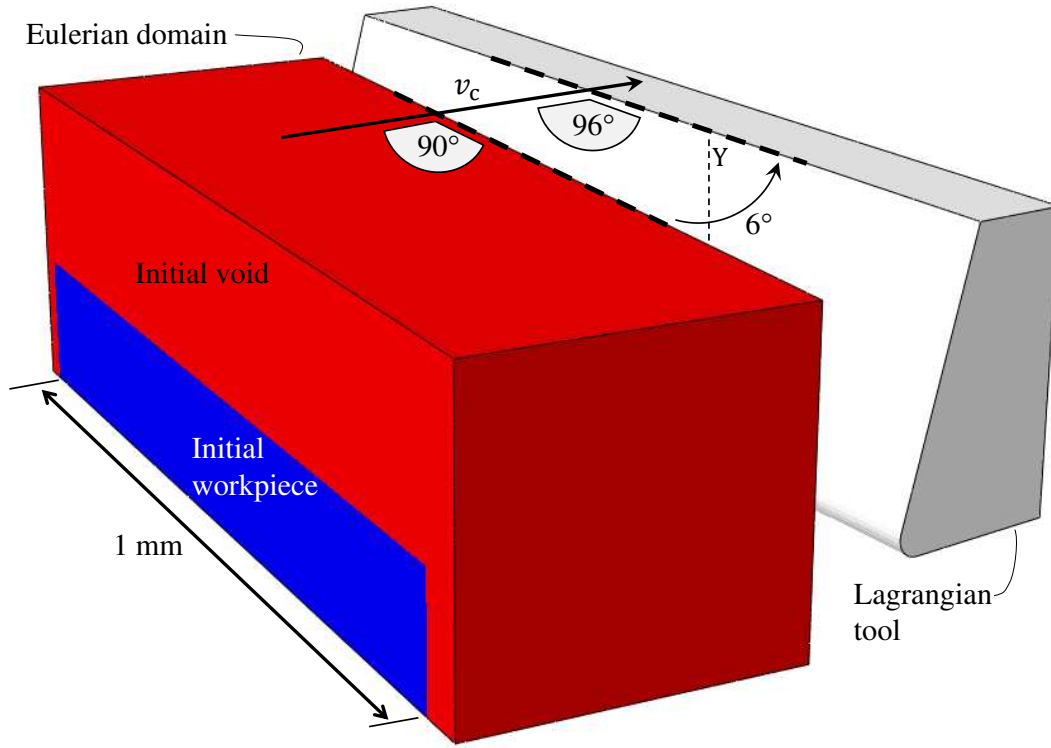


Figure 3: Configuration of the FE model for $\lambda_s = 6^\circ$

131 The Ti6Al4V workpiece is assumed to be thermo-elasto-viscoplastic (isotropic)
 132 and inelastic heat fraction is 0.9. JC set of parameters from Seo et al. [27] is
 133 adopted as the value of A corresponds to the typical yield stress value of Ti6Al4V
 134 and this set proved to provide the best results among 20 sets available in the lit-
 135 erature [28]. The tungsten carbide tool with TiN coating is assumed to be linear
 136 elastic. Material properties are provided in Table 2.

Following the experimental results of Rech et al. [31], Coulomb's friction is assumed to occur at the tool-workpiece interface and both friction, μ , and heat partition, β , coefficients depend on the cutting speed. Limiting shear stress, τ_{\max} , is included and is given by

$$\tau_{\max} = \frac{\text{yield stress}}{\sqrt{3}} = \frac{A}{\sqrt{3}} \quad (2)$$

137 All the friction energy is converted into heat. Table 3 shows the friction coeffi-
 138 cients adopted in this study.

Table 2: Materials properties [27, 29, 30]

Young's modulus, E (GPa)	Ti6Al4V	113.8*
	WC	650
Poisson's ratio, ν	Ti6Al4V	0.34
	WC	0.2
Density, ρ (kg/m ³)	Ti6Al4V	4,430
	WC	14,850
Conductivity, k (W/mK)	Ti6Al4V	6.3*
	WC	100
Expansion, α (K ⁻¹)	Ti6Al4V	8.6 e ⁻⁶ *
	WC	5 e ⁻⁶
Specific heat, c_p (J/KgK)	Ti6Al4V	531*
	WC	202
JC constitutive model	A (MPa)	997.9
	B (MPa)	653.1
	C	0.0198
	m	0.7
	n	0.45
	$\dot{\epsilon}_0$ (s ⁻¹)	1
	T_{room} (K)	293
	T_{melt} (K)	1873

*: Dependence to the temperature, value provided at 293 K

139 Room temperature of 293 K is imposed on the upper and right surfaces of the
140 tool and on the left and bottom surfaces of the workpiece (Figure 2). Radiation
141 and convection are assumed to occur on the rake and clearance faces of the tool.
142 Initial temperature of the tool and the workpiece is set to room temperature (293
143 K). Heat transfer coefficients are provided in Table 3.

144 3.2. Material constitutive model of Ti6Al4V

145 The constitutive model of the Ti6Al4V material used in all the numerical sim-
146 ulations proposed in section 4 is a thermo-elasto-viscoplastic law using a flow cri-
147 terion based on an ANN identified for the selected material and implemented in
148 the Abaqus/Explicit code via a Fortran routine VUHARD as proposed by Pantalé
149 et al. in [26]. The principle of this approach consists in replacing the analyti-
150 cal formulation of the flow law, based on a Johnson-Cook or Zerilli-Armstrong

Table 3: Friction and heat transfer coefficients [29, 31]

Cutting speed, v_c (m/min)	μ	β
5	0.24	1
7.5	0.22	0.89
10	0.21	0.80
20	0.19	0.63
30	0.18	0.55
40	0.17	0.50
Limiting shear stress, τ_{\max} (MPa)	576	
Convection, U (W/m ² K)	50	
Radiation, ϵ	0.3	

151 type model, and allowing the calculation of the flow stress σ^y as a function of the
152 plastic strain ε^p , of the plastic strain rate, $\dot{\varepsilon}^p$, and of the temperature T , by a multi-
153 layer ANN serving as universal approximator. Thus, the parameters of the neural
154 network can directly be identified from the experimental data without having to
155 postulate a behavioural model, which simplifies the procedure and allows more
156 flexibility in the definition of the model. The proposed approach also allows, as
157 shown in Pantalé et al. [26], to compute the derivatives of the flow stress σ^y with
158 respect to the three input variables of the model, a necessary step to implement this
159 model as a flow law in the form of a VUHARD subroutine in the Abaqus/Explicit
160 FEM code.

161 In order to verify the influence of the complexity of the neural network on the
162 numerical results of the simulation and the computing time, several architectures
163 of ANN are tested thereafter (in 3.4). The chosen global architecture has 2 hidden
164 layers with a variable number of neurons for the first hidden layer ($\zeta = 9$ to 17)
165 and 7 neurons for the second hidden layer, 3 inputs (plastic strain, ε^p , plastic
166 strain rate, $\dot{\varepsilon}^p$, and temperature, T) and one output (the yield stress, σ^y). The
167 global architecture of this kind of ANN is given in Figure 4 for 9 neurons in
168 the first hidden layer. Conforming to Pantalé et al. [26], this ANN is referred
169 after the terminology ANN 3-9-7-1-sig, because it has 3 inputs, 9 neurons in the
170 first hidden layer, 7 neurons in the second hidden layer, 1 output and a sigmoid
171 activation function.

172 The main advantage of this approach (the use of an ANN), after the training
173 phase, is that the output σ^y of the network is related to the inputs ε^p , $\dot{\varepsilon}^p$, and T

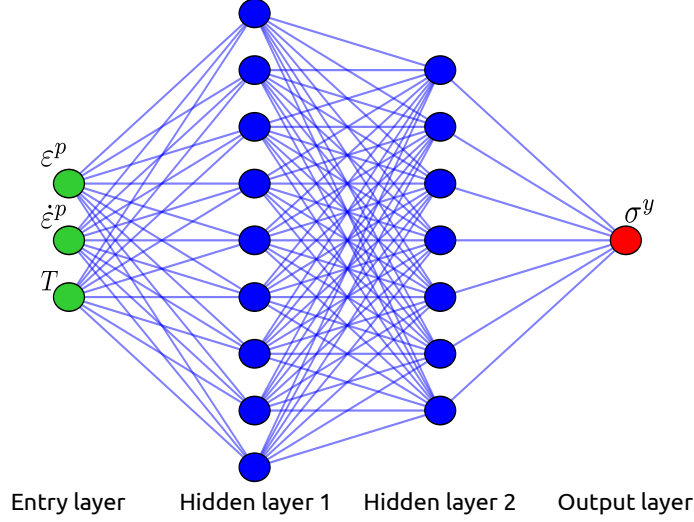


Figure 4: Architecture of the ANN 3-9-7-1-sig used for the flow law

174 through equations (3) to (7). The first step is to scale the input data to the interval
 175 $[0, 1]$ using the following equation:

$$\vec{x} = \begin{cases} x_1 = \frac{\varepsilon^p - [\varepsilon^p]_{min}}{[\varepsilon^p]_{max} - [\varepsilon^p]_{min}} \\ x_2 = \frac{\ln(\varepsilon^p) - [\ln(\varepsilon^p)]_{min}}{[\ln(\varepsilon^p)]_{max} - [\ln(\varepsilon^p)]_{min}} \\ x_3 = \frac{T - [T]_{min}}{[T]_{max} - [T]_{min}} \end{cases} \quad (3)$$

176 The outputs of the neurons in the first hidden layer are given by the following
 177 equation:

$$\vec{y}_1 = \text{sig}(\mathbf{w}_1 \cdot \vec{x} + \vec{b}_1) \quad (4)$$

where, $\text{sig}()$ is the sigmoid activation function defined by equation (5):

$$\text{sig}(x) = \frac{1}{1 + e^{-x}} \quad (5)$$

Then, the output of the neurons in the second hidden layer are given by equation (6):

$$\vec{y}_2 = \text{sig}(\mathbf{w}_2 \cdot \vec{y}_1 + \vec{b}_2) \quad (6)$$

So, the output of the ANN is therefore given by equation (7).

$$\sigma = ([\sigma]_{max} - [\sigma]_{min}) (\vec{w}^T \cdot \vec{y}_2 + b) + [\sigma]_{min} \quad (7)$$

178 In equations (3) to (7), quantities \mathbf{W}_1 , \mathbf{W}_2 , \vec{w} , \vec{b}_1 , \vec{b}_2 and b are given by the
 179 training procedure of the ANN. Corresponding values for an ANN containing 9
 180 neurons in the first hidden layer are reported in Appendix A. Quantities $[\]_{min}$ and
 181 $[\]_{max}$ are the boundaries of the range of the corresponding field during the training
 182 phase, values are also given in Appendix A.

183 Because of the large number of identified parameters for all the ANN models
 184 (from 114 to 202 for 9 and 17 neurons for the first hidden layer, respectively);
 185 the other 4 sets of ANN parameters used in this publication can be found in [32].
 186 [FD:] Inclure dans corps du texte puisque article normal et rq reviewer?

187 3.3. Sensitivity study of the results to mass scaling

FE modelling of the cutting process is very expensive in CPU computation time because of the coupling in many nonlinear phenomena and the large amount of tiny finite elements. Mass scaling (MS) is introduced in the model to reduce the CPU computation time while checking that it does not influence the results (forces and energies) via a mass scaling sensitivity study. MS factors, MS_f , ranging from 1E6 (theoretical scaling of CPU time of $\sqrt{MS_f} = 1000$) to 1 (no scaling) have been used for one cutting condition ($\lambda_s = 0^\circ$, $v_c = 30$ m/min and $h = 60$ μ m). The same signal processing procedure is applied to the numerical forces as to the experimental forces (cf. 2): they are filtered with a second-order low-pass Bessel filter at 750 Hz before computing the mean value at steady state. Table 4 gives the results normalised (\hat{F}_i) by these of the model without MS:

$$\hat{F}_i = \frac{F_i \text{ with MS}}{F_i \text{ without MS}} \quad (8)$$

188 With $i = c$ for the cutting force and $i = f$ for the feed force. As expected,
 189 actual speed-up does not increase linearly with the MS_f , but it is still significant.
 190 MS_f of 1E6 leads to unstable computation and MS_f of 1E5 results in erratic
 191 forces evolutions. These results are confirmed by high values of the kinetic (KE)
 192 on internal (IE) energies ratio (it should not exceed a few % [33, 34]). A MS_f
 193 value of 1E3 is selected as it provides a good balance between computation time
 194 reduction and impact on forces, while keeping $\frac{KE}{IE}$ below 1%. To provide an order
 195 of magnitude of CPU computation time, between 10 h and 50 h (depending on the
 196 value of h) are needed on 4 cores of an Intel i7-5700HQ CPU at 2.7 – 3.5 GHz.

197 3.4. Sensitivity study of the results to the number of neurons

The number of neurons on the hidden layers may influence the results. A sensitivity study on the number of neurons for the first hidden layer, ζ , is carried

Table 4: MS sensitivity study (selected MS factor, MS_f , in bold, \hat{F}_c : normalized cutting force, \hat{F}_f : normalized feed force, KE : kinetic energy, IE : internal energy)

MS_f	CPU scaling	Speed-up	\hat{F}_c	\hat{F}_f	$\frac{KE}{IE}$ (%)
1	1	1	1	1	2.3E-4
1E2	10	9	1.006	0.982	2.2E-2
1E3	32	21	1.008	0.940	2.2E-1
1E4	100	61	1.012	0.921	2.4
1E5	316	173	Erratic	Erratic	22
1E6	1000	207	Unstable	Unstable	58

out to select the ANN providing the best balance between CPU computation time and quality of the results. The results of the study are provided in Table 5. \check{F}_i corresponds to the results normalised by these of the model with the built-in JC model:

$$\check{F}_i = \frac{F_i \text{ with ANN}}{F_i \text{ with JC}} \quad (9)$$

198 They show no influence on the forces when compared to the built-in Johnson-
199 Cook model, only computation time is influenced. A first hidden layer with 9
200 neurons is therefore selected as it leads to the lowest CPU computation time in-
201 crease.

Table 5: Sensitivity of the forces to the number of neurons of the first layer, ζ (selection in bold, \check{F}_c : normalized cutting force, \check{F}_f : normalized feed force)

ζ	Time increase (%)	\check{F}_c	\check{F}_f
Built-in	0	1.000	1.000
9	6	1.000	0.999
11	6	1.001	1.000
13	7	1.000	0.998
15	8	1.001	1.001
17	10	1.000	1.000

202 4. Experimental and numerical results

203 [FD:] Show chips? + info on side flow? + dedicated subsection on chip thick-
 204 ness? (give also results in a plot?) Mean and standard deviation (2σ) are computed
 205 from the 3 experimental values and are shown in Figures 5 to 7. Mean numerical
 206 values are plotted inside the experimental bars in Figures 5 to 7. [FD:] sigma deja
 207 utilise mais equa (5) devrait etre sigma y - voir avec Olivier [FD:] Add a table
 208 with mean differences as a kind of summary of the results?

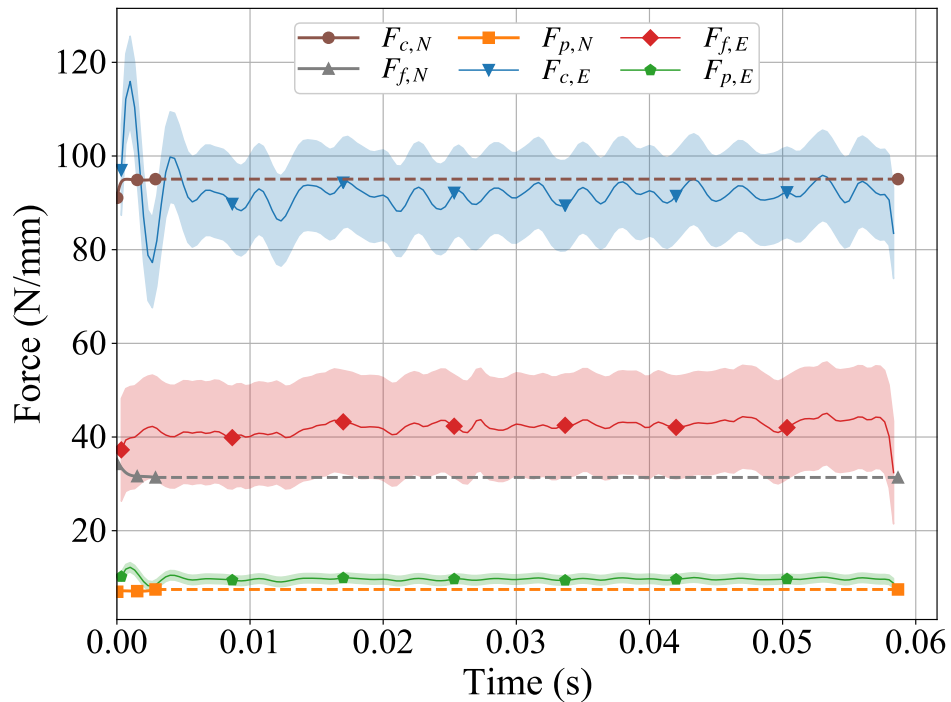


Figure 5: Temporal evolutions of experimental (E) and numerical (N) forces at 6°, 10 m/min and 40 μm: dispersion around mean experimental values and linear extrapolation of numerical values in dashed

209 + fig with sim chip and show that it is helical/spiral at 6 deg + Chip thickness
 210 is globally lower at 6 deg than 0 deg + Show side flow, non-uniform chip thickness

211 The increase of the cutting force with the uncut chip thickness is clearly ob-
 212 served in Figure 5 for both experimental and numerical results at the 2 inclina-
 213 tion angles, as well as the decrease of the force with the increase in the cutting

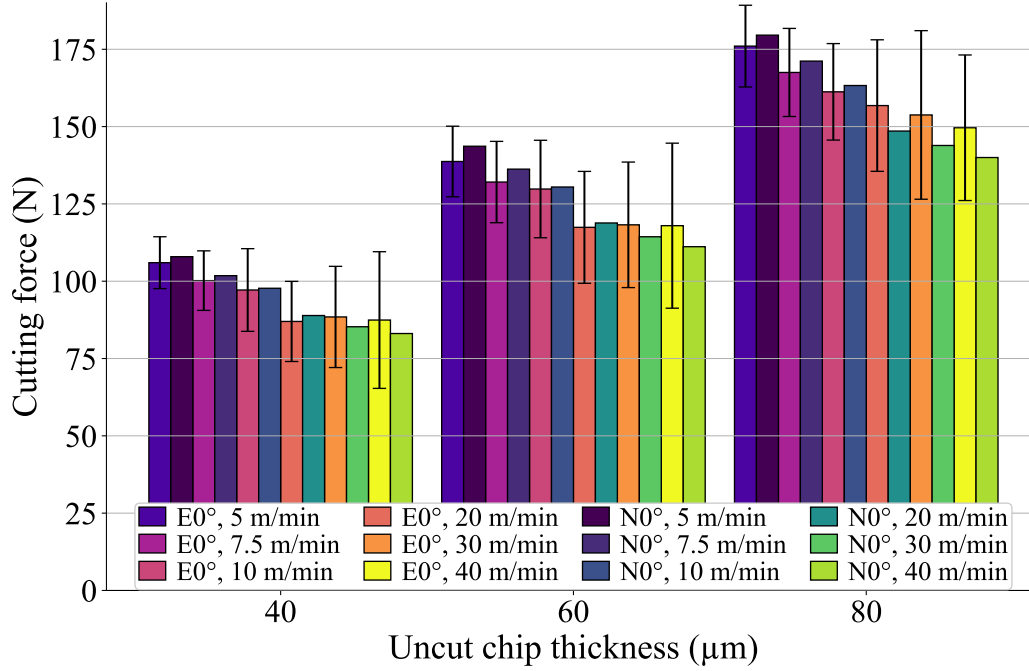


Figure 6: Comparison of experimental (E) and numerical (N) cutting forces at 0°

[FD:] Better explain legend in caption, same for other figures

214 speed. This shows temperature softening domination on strain rate hardening for
 215 Ti6Al4V and that it is accurately modelled. The increase of the inclination angle
 216 from 0° to 6° reduces the cutting force; this is well captured by the model.
 217 For cutting speeds of 20-40 m/min, F_c is almost constant for 40 μm and 60 μm,
 218 while it slightly decreases for 80 μm; this small stabilisation is less marked for the
 219 model. Increase in the deviation around the mean value with the cutting speed is
 220 noted for values above 10 m/min. All numerical values are within a confidence in-
 221 terval of 95% of the experiments (35 out of 36 conditions are within a confidence
 222 interval of 68%) and the mean difference with the experiments is 3%, which is re-
 223 markable, moreover given the wide range of cutting conditions considered. This
 224 highlights the predictive qualities of the FE model for both inclination angles.
 225 Figure 6 shows the results for the feed force, where the two clearest trends are
 226 its decrease with inclination angle and its increase with the uncut chip thickness
 227 for both experimental and numerical results. For 80 μm, F_f globally decreases
 228 with v_c in the experiments. For 40 and 60 μm, the force decreases at lower v_c

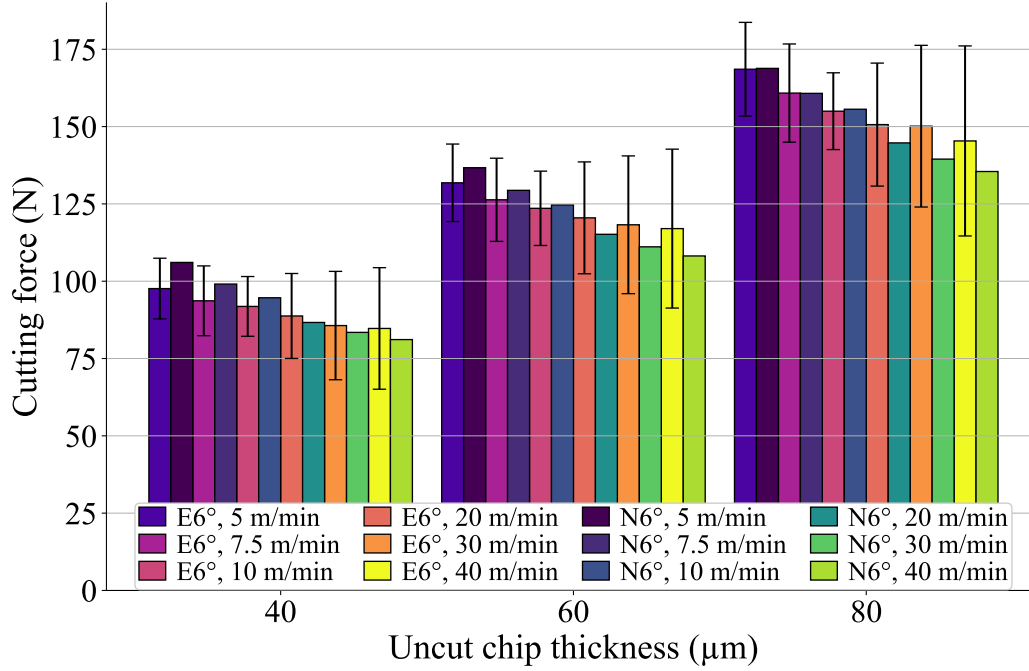


Figure 7: Comparison of experimental (E) and numerical (N) cutting forces at 6°

229 and then increases for 0°, while a decrease is observed at all v_c for 6°. For the
 230 numerical values, the global trend is the same for the 3 uncut chip thicknesses and
 231 both inclination angles: a decrease for the lowest v_c values and then an increase.
 232 The numerical values are mostly not within the 95% confidence interval (it has
 233 no clear evolution with the cutting conditions). Coupled with the differences in
 234 trends, it shows that F_f is less well modelled (mean difference is 35%) as usual in
 235 FE modelling of the cutting process. Improving the friction model should enhance
 236 the results. Passive force is non-zero for the inclination angle of 6° (Figure 7). As
 237 the cutting force, it increases with the uncut chip thickness and it decreases with
 238 the cutting speed. Comparison with the experiments is globally the same as for
 239 F_c , except for a larger difference in the magnitude of F_p (mean difference is 26%,
 240 but it is small in absolute – less than 5 N). The numerical values are mostly not
 241 in the 95% experimental confidence interval. Regarding the chips morphology,
 242 all of them are continuous. For both the simulation and the experiments, the chip
 243 thickness ratio, λ_h , decreases with the cutting speed because of reduction of fric-
 244 tion and it is almost independent of the uncut chip thickness. The mean difference

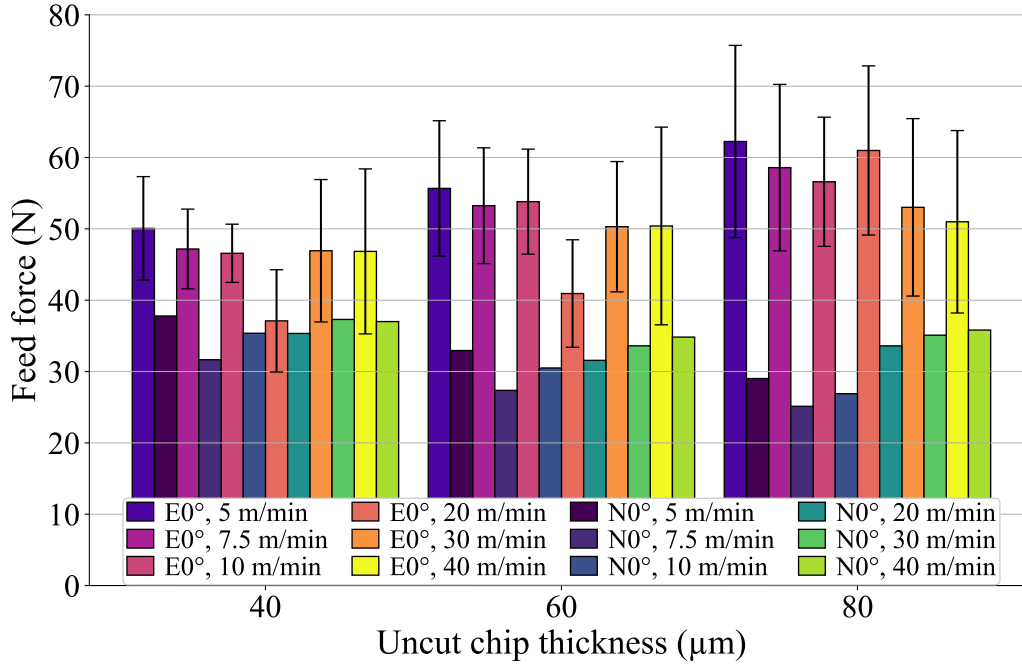


Figure 8: Comparison of experimental (E) and numerical (N) feed forces at 0°

245 between experimental and numerical λ_h is 13% across the whole range of cutting
 246 conditions.

247 [FD:] Check clearly stated that Ff trend is globally NOK: improve friction and
 248 mat para also cf. Metals Kuga + increase with h quite low in the exp.

249 5. Conclusions

250 In this paper, an experimental study has been carried out in free orthogonal
 251 and oblique cutting for Ti6Al4V. It is a reference to assess the performances of
 252 the 3D FE model introducing an ANN-based constitutive model and developed
 253 in the same conditions. An unpreviously seen wide range of cutting conditions,
 254 36, is considered, including 2 inclination angles. Accurate evaluation of funda-
 255 mental variables in 3D with the absence of tuning of both numerical parameters
 256 and model features when cutting conditions and inclination angle are significantly
 257 modified is a strong novelty of this work. Only changing the inclination angle to
 258 move from free orthogonal to oblique cutting while maintaining the quality of the
 259 results has no equivalent in the current literature, moreover as no study on free

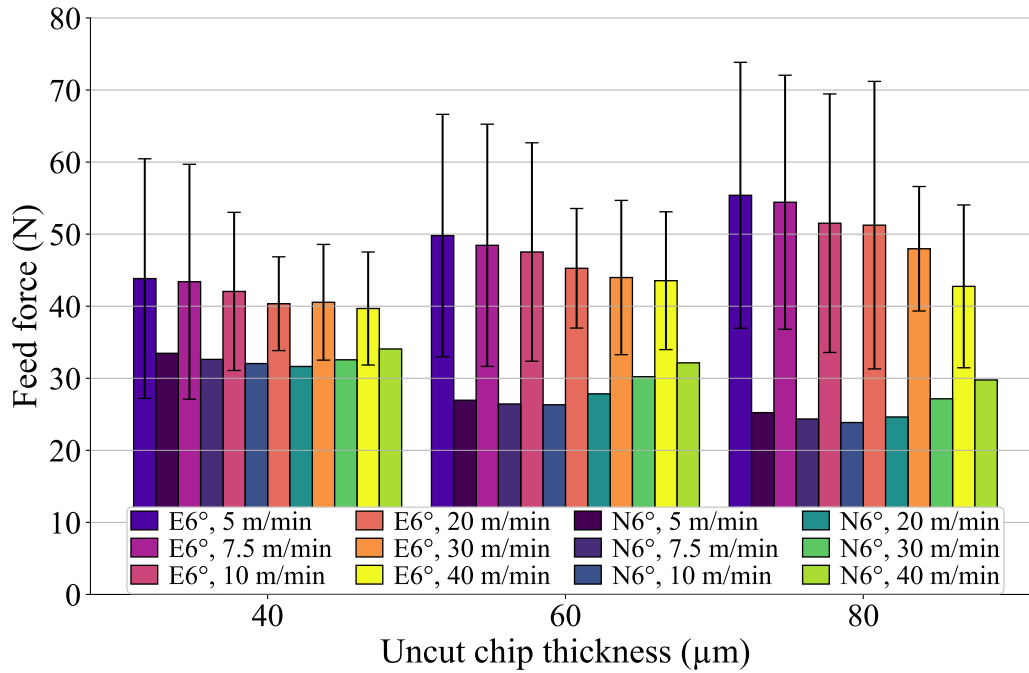


Figure 9: Comparison of experimental (E) and numerical (N) feed forces at 6°

oblique cutting is available. Predictive abilities of the model make it adequate for development of tools with a straight cutting edge, for example.

this works opens possibilities in both 3D free orthogonal cutting and ANN based material behaviours

References

- [1] P. J. Arrazola, T. Özel, D. Umbrello, M. Davies, I. S. Jawahir, Recent advances in modelling of metal machining processes, *CIRP Annals* 62 (2013) 695–718.
- [2] M. Agmell, V. Bushlya, S. V. A. Laakso, A. Ahadi, J.-E. Ståhl, Development of a simulation model to study tool loads in pcBN when machining AISI 316L, *Int J Adv Manuf Technol* 96 (2018) 2853–2865.
- [3] X. Xu, J. Outeiro, J. Zhang, B. Li, W. Zhao, Simulation of material side flow using a 3D coupled Eulerian-Lagrangian approach and a constitutive model considering the stress state, *Procedia CIRP* 102 (2021) 441–446.

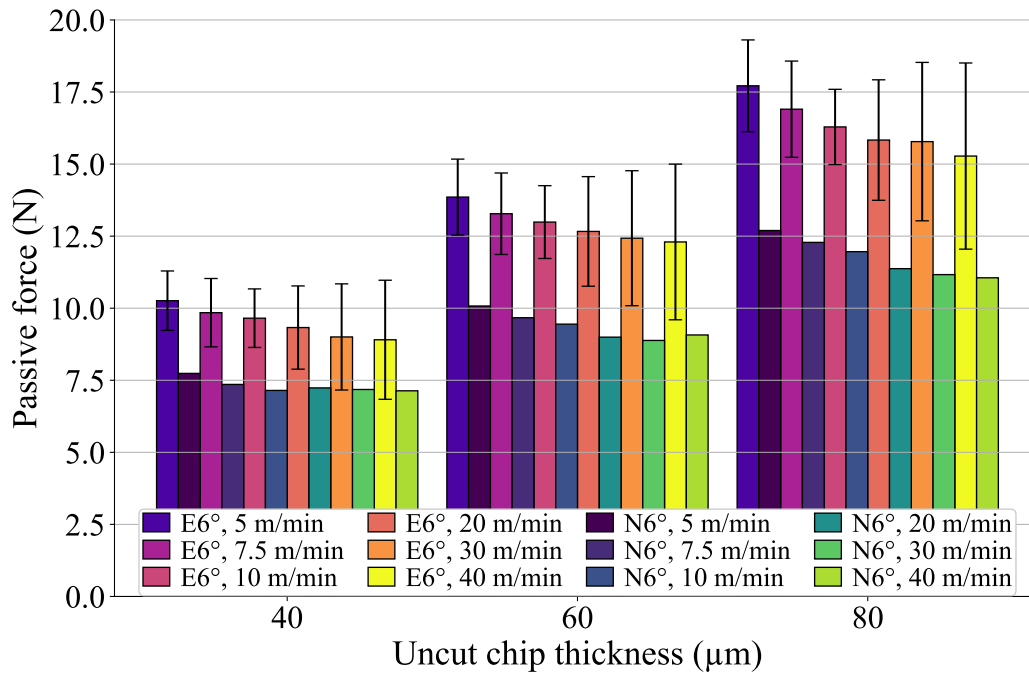


Figure 10: Comparison of experimental (E) and numerical (N) passive forces at 6°

- 274 [4] M. Abouridouane, T. Bergs, D. Schraknepper, G. Wirtz, Friction behavior
 275 in metal cutting: Modeling and simulation, *Procedia CIRP* 102 (2021) 405–
 276 410.
- 277 [5] F. Ducobu, E. Rivière-Lorphèvre, E. Filippi, Experimental contribution to
 278 the study of the Ti6Al4V chip formation in orthogonal cutting on a milling
 279 machine, *Int J Mater Form* 8 (2015) 455–468.
- 280 [6] A. Sela, G. Ortiz-de-Zarate, D. Soler, G. Germain, P. Aristimuño, P. J. Arra-
 281 zola, Measurement of plastic strain and plastic strain rate during orthogonal
 282 cutting for Ti-6Al-4V, *International Journal of Mechanical Sciences* 198
 283 (2021) 106397.
- 284 [7] M. Afrasiabi, J. Saelzer, S. Berger, I. Iovkov, H. Klippel, M. Röthlin,
 285 A. Zabel, D. Biermann, K. Wegener, A Numerical-Experimental Study on
 286 Orthogonal Cutting of AISI 1045 Steel and Ti6Al4V Alloy: SPH and FEM
 287 Modeling with Newly Identified Friction Coefficients, *Metals* 11 (2021)
 288 1683.

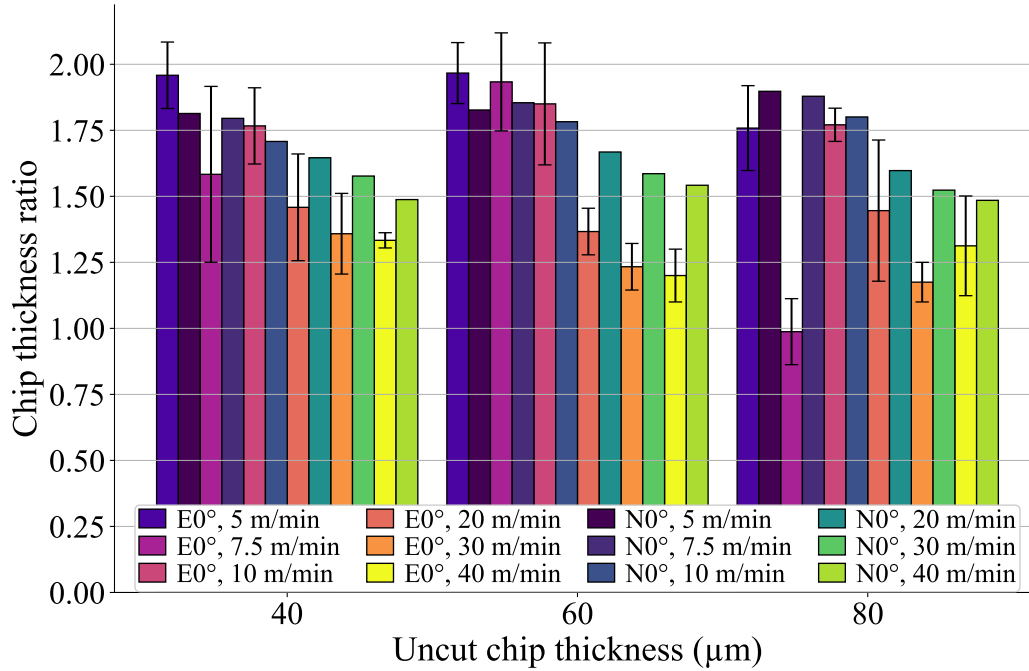


Figure 11: Comparison of experimental (E) and numerical (N) chip thickness ratios at 0°

- 289 [8] F. Ducobu, E. Rivière-Lorphèvre, E. Filippi, Application of the Coupled
 290 Eulerian-Lagrangian (CEL) method to the modeling of orthogonal cutting,
 291 Eur J Mech A Solids 59 (2016) 58–66.
- 292 [9] F. Ducobu, E. Rivière-Lorphèvre, E. Filippi, Finite element modelling of 3D
 293 orthogonal cutting experimental tests with the Coupled Eulerian-Lagrangian
 294 (CEL) formulation, Finite Elements in Analysis and Design 134 (2017) 27–
 295 40.
- 296 [10] D. Ambrosio, A. Tongne, V. Wagner, G. Dessein, O. Cahuc, A new damage
 297 evolution criterion for the coupled Eulerian-Lagrangian approach: Applica-
 298 tion to three-dimensional numerical simulation of segmented chip formation
 299 mechanisms in orthogonal cutting, Journal of Manufacturing Processes 73
 300 (2022) 149–163.
- 301 [11] A. Vovk, J. Sölter, B. Karpuschewski, Finite element simulations of the
 302 material loads and residual stresses in milling utilizing the CEL method,
 303 Procedia CIRP 87 (2020) 539–544.

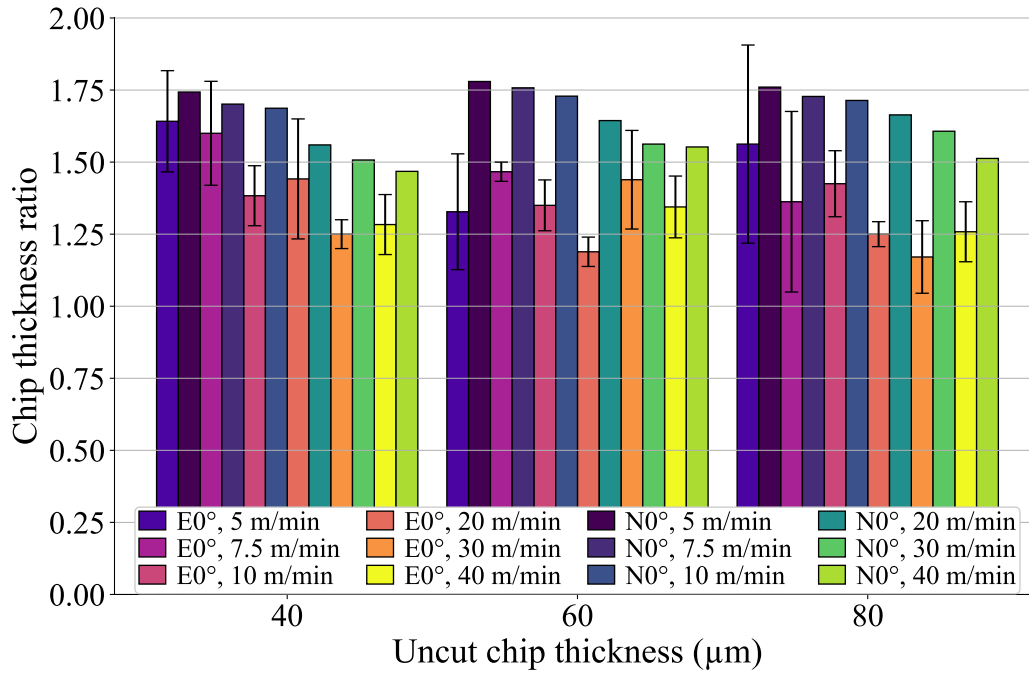


Figure 12: Comparison of experimental (E) and numerical (N) chip thickness ratios at 6°

- [12] M. Hardt, T. Berghs, Three Dimensional Numerical Modeling of Face Turning Using the Coupled-Eulerian-Lagrangian Formulation, *Procedia CIRP* 102 (2021) 162–167.
- [13] S. N. Melkote, W. Grzesik, J. Outeiro, J. Rech, V. Schulze, H. Attia, P.-J. Arrazola, R. M'Saoubi, C. Saldana, Advances in material and friction data for modelling of metal machining, *CIRP Annals* 66 (2017) 731–754.
- [14] G. Johnson, W. Cook, A constitutive model and data for metals subjected to large strains, high strain rates and high temperatures, in: *Proc. 7th International Symposium on Ballistics*, volume 21, The Hague, The Netherlands, pp. 541–547.
- [15] M. Calamaz, D. Coupard, F. Girot, A new material model for 2D numerical simulation of serrated chip formation when machining titanium alloy Ti-6Al-4V, *International Journal of Machine Tools and Manufacture* 48 (2008) 275–288.

- 318 [16] T. Özel, T. Altan, Determination of workpiece flow stress and friction at the
319 chip–tool contact for high-speed cutting, *Int J Mach Tools Manuf* 40 (2000)
320 133–152.
- 321 [17] A. Shrot, M. Bäker, Determination of Johnson–Cook parameters from ma-
322 chining simulations, *Comput Mater Sci* 52 (2012) 298–304.
- 323 [18] F. Klocke, D. Lung, S. Buchkremer, I. S. Jawahir, From Orthogonal Cutting
324 Experiments towards Easy-to-Implement and Accurate Flow Stress Data,
325 *Materials and Manufacturing Processes* 28 (2013) 1222–1227.
- 326 [19] P. Bosetti, C. Maximiliano Giorgio Bort, S. Bruschi, Identification of John-
327 son–Cook and Tresca’s Parameters for Numerical Modeling of AISI-304
328 Machining Processes, *J Manuf Sci Eng* 135 (2013).
- 329 [20] B. Denkena, T. Grove, M. A. Dittrich, D. Niederwestberg, M. Lahres, In-
330 verse Determination of Constitutive Equations and Cutting Force Modelling
331 for Complex Tools Using Oxley’s Predictive Machining Theory, *Procedia*
332 *CIRP* 31 (2015) 405–410.
- 333 [21] T. Bergs, M. Hardt, D. Schraknepper, Determination of Johnson-Cook ma-
334 terial model parameters for AISI 1045 from orthogonal cutting tests using
335 the Downhill-Simplex algorithm, *Procedia Manuf* 48 (2020) 541–552.
- 336 [22] M. Hardt, D. Schraknepper, T. Bergs, Investigations on the Application of
337 the Downhill-Simplex-Algorithm to the Inverse Determination of Material
338 Model Parameters for FE-Machining Simulations, *Simulation Modelling*
339 *Practice and Theory* 107 (2021) 102214.
- 340 [23] B. Stampfer, G. González, E. Segebade, M. Gerstenmeyer, V. Schulze, Ma-
341 terial parameter optimization for orthogonal cutting simulations of AISI4140
342 at various tempering conditions, *Procedia CIRP* 102 (2021) 198–203.
- 343 [24] M. Hardt, D. Jayaramaiah, T. Bergs, On the Application of the Particle
344 Swarm Optimization to the Inverse Determination of Material Model Pa-
345 rameters for Cutting Simulations, *Modelling* 2 (2021) 129–148.
- 346 [25] N. Kugalur Palanisamy, E. Rivière Lorphèvre, M. Gobert, G. Briffoteaux,
347 D. Tuytens, P.-J. Arrazola, F. Ducobu, Identification of the Parameter Val-
348 ues of the Constitutive and Friction Models in Machining Using EGO Algo-
349 rithm: Application to Ti6Al4V, *Metals* 12 (2022) 976.

- [26] O. Pantalé, P. Tize Mha, A. Tongne, Efficient implementation of non-linear flow law using neural network into the Abaqus Explicit FEM code, *Finite Elements in Analysis and Design* 198 (2022) 103647.
- [27] S. Seo, O. Min, H. Yang, Constitutive equation for Ti–6Al–4V at high temperatures measured using the SHPB technique, *Int J Impact Eng* 31 (2005) 735–754.
- [28] F. Ducobu, E. Rivière-Lorphèvre, E. Filippi, On the importance of the choice of the parameters of the Johnson-Cook constitutive model and their influence on the results of a Ti6Al4V orthogonal cutting model, *Int J Mech Sci* 122 (2017) 143–155.
- [29] GRANTA EduPack 2020, Granta Design Limited, 2020.
- [30] N. Milošević, I. Aleksic, Thermophysical properties of solid phase Ti-6Al-4V alloy over a wide temperature range (2012).
- [31] J. Rech, P. J. Arrazola, C. Claudin, C. Courbon, F. Pusavec, J. Kopac, Characterisation of friction and heat partition coefficients at the tool-work material interface in cutting, *CIRP Annals* 62 (2013) 79–82.
- [32] O. Pantalé, Coefficients of an ANN constitutive flow law of a Ti6-Al-4V material for dynamic applications, Zenodo (2022).
- [33] L. Wang, H. Long, Investigation of material deformation in multi-pass conventional metal spinning, *Materials & Design* 32 (2011) 2891–2899.
- [34] F. Ducobu, E. Rivière-Lorphèvre, E. Filippi, On the introduction of adaptive mass scaling in a finite element model of Ti6Al4V orthogonal cutting, *Simulation Modelling Practice and Theory* 53 (2015) 1–14.

Appendix A. Coefficients of the ANN 3-9-7-1-sig

In this Appendix, we present the values obtained after the training phase of an ANN containing 9 neurons in the first hidden layer and 7 neurons in the second hidden layer.

The training of the neural network was performed using a data set containing 3 430 data points defined by: [FD:] Add units for min and max values?

- 70 values for $\varepsilon^p \in [0.0, 3.0]$, so that $[\varepsilon^p]_{min} = 0$ and $[\varepsilon^p]_{max} = 3$.

- 7 plastic strain rates $\dot{\epsilon}^p \in [1, 10, 50, 500, 5\,000, 50\,000, 500\,000]$, so that $[\ln(\dot{\epsilon}^p)]_{min} = 0$ and $[\ln(\dot{\epsilon}^p)]_{max} = 13.12236$.
- 7 temperatures $T \in [293, 400, 500, 700, 900, 1\,200, 1\,500]$, so that $[T]_{min} = 293$ and $[T]_{max} = 1\,500$.

Stresses in the training dataset ranges from $[\sigma]_{min} = 171.44$ to $[\sigma]_{max} = 2606.12$. The results of the training process are given below for quantities \mathbf{W}_1 , \mathbf{W}_2 , \vec{w} , \vec{b}_1 , \vec{b}_2 and b . [FD:] sigma y?

$$\mathbf{W}_1 = \begin{bmatrix} -0.87229 & -0.47675 & -1.50771 \\ -0.95762 & -0.25619 & 1.65222 \\ -10.61660 & 0.22003 & -0.11539 \\ 3.67883 & 0.37146 & -1.51069 \\ -63.39468 & 0.15466 & -0.95431 \\ 0.54807 & 0.25959 & -5.44355 \\ -1.33883 & 0.36089 & -1.66735 \\ -0.68125 & 1.02121 & 0.34242 \\ 0.08740 & 0.18764 & -41.32542 \end{bmatrix}$$

$$\mathbf{W}_2^T = \begin{bmatrix} 1.66285 & -0.59645 & -3.17333 & 0.20706 & 1.18760 & 2.01250 & -0.82147 \\ -0.26237 & -2.50330 & -1.45941 & -1.59833 & 4.05169 & -1.21146 & 1.05610 \\ -0.12958 & 0.67119 & -5.85989 & -2.55061 & 4.85245 & 4.31876 & 3.24070 \\ -2.12890 & 0.68296 & 0.71183 & 0.81706 & -0.09405 & 0.34919 & -1.41223 \\ 2.33631 & -0.08089 & 14.65789 & 0.12531 & 23.66363 & 2.55872 & 2.15338 \\ 0.11567 & 1.77629 & -1.80448 & 0.77825 & -1.58254 & 1.90442 & 1.23152 \\ 1.49265 & 0.41821 & -3.53803 & -0.48705 & -0.23671 & 0.75887 & -0.37441 \\ 0.95990 & 0.69041 & 0.43870 & 0.28393 & -1.40101 & -0.64569 & -0.38964 \\ 5.89937 & -0.13015 & 2.99264 & 1.78534 & -3.90189 & 1.17494 & -3.78854 \end{bmatrix}$$

$$\vec{w} = \begin{bmatrix} 0.34701 \\ 1.42079 \\ -0.96564 \\ 0.62467 \\ -0.56322 \\ 0.40960 \\ -0.42810 \end{bmatrix}$$

$$\vec{b}_1 = \begin{bmatrix} 2.57141 \\ 0.22673 \\ -1.16985 \\ -0.11246 \\ -0.82210 \\ -2.13264 \\ 0.78794 \\ 1.20434 \\ -3.48681 \end{bmatrix}$$

$$\vec{b}_2 = \begin{bmatrix} -0.36566 \\ -1.14445 \\ -0.79065 \\ -0.50670 \\ 1.30136 \\ 0.04521 \\ -0.29995 \end{bmatrix}$$

$$b = 0.04213$$